Low-Power Underwater Acoustic Tracers for Long-Range River Bedload Monitoring

Peter Oppermann
Institute for Autonomous Cyber-Physical Systems,
Hamburg University of Technology
DE
peter.oppermann@tuhh.de

Bernd-Christian Renner
Institute for Autonomous Cyber-Physical Systems,
Hamburg University of Technology (TUHH)
DE
christian.renner@tuhh.de

Abstract

Understanding sediment transport (bedload) in rivers and streams is crucial for maintaining navigable waterways and ecological health. Unlike traditional localized sampling, tracers offer broader insights. This paper extends our efforts to overcome the limitations of RF tracers, which suffer from significant signal attenuation in water. We present a low-power underwater acoustic tracer utilizing an improved piezo driver with resonance-switching. The proposed tracers generate signals four times stronger than our previous prototype, enabling detection over distances up to 400 meters, a substantial improvement from the prior 200-meter limit. Simulation and real-world tests demonstrate robustness against Doppler shifts and moderate multipath propagation. Compact and costing only 15 € (including the transducer), the prototype promises year-long operation on a small battery. The technology also holds potential for diverse applications, including environmental monitoring, diver localization, or aquatic wildlife tracking.

ACM Reference Format:
Peter Oppermann and Bernd-Christian Renner. 2024. Low-Power Underwater Acoustic Tracers for Long-Range River Bedload Monitoring. In *The 18th ACM International Conference on Underwater Networks & Systems (WUWNET '24), October 28–31, 2024, Sibenik, Croatia.* ACM, New York, NY, USA, 8 pages. https://doi.org/10.1145/3699432.3699469

1 Introduction

Understanding sediment transport (bedload) in rivers and streams is essential for keeping waterways navigable and maintaining ecological health. Conventional methods for measuring bedload transport often involve localized sampling techniques, such as bedload traps or monitoring particle movement through backscattered sound or laser diffraction. However, these methods yield sparse data confined to the vicinity of the sampling sites [17, 23].

Alternatively, bedload tracers that mimic natural sediment particles can address these shortcomings. By deploying and tracking large quantities of these tracers, researchers can obtain comprehensive statistical data on sediment movement patterns [14, 16]. Initially, tracers emitting nuclear or radio-frequency (RF) signals were employed. However, radioactive tracers have been largely discontinued due to environmental concerns. Instead, RF signals are used but limited by significant attenuation in water, making them suitable only in shallow depths.

To compete with the state-of-the-art RF tracers, acoustic tracers must be

- small (down to 40x20x20 mm^3),
- affordable (costing tens of euros each),
- durable (lasting at least six months on a battery),
- detectable over long distances ($\geq$ 50 m), and,
- suitable for accurate localization.

In a pilot study [18], we explored acoustic signals for bedload tracing, addressing the limitations of current RF-based methods, and presented a minimalistic tracer prototype. While the results were promising, the study showed that the tracer had insufficient signal power for detection over more than 75 m in the presence of river noise, and 200 m in a tranquil lake. Moreover, the unknown transducer directionality complicates range estimation when the tracer is misaligned with the receiver. This work presents an improved piezo driver based on resonance-switching that can generate four times stronger signals while being more efficient. With the improved signal power, we reach transmission distances of up to 400 m in a tranquil canal. Furthermore, we analyze transducer characteristics and evaluate robustness against Doppler frequency shifts and multipath propagation in a simulation study. We also analyze power consumption, showing runtimes exceeding a year are feasible.

Beyond sediment tracing, ultra-low-cost acoustic beacons have diverse applications, including locating sunken vessels or aircrafts, environmental monitoring with submerged sensors, and tracking aquatic wildlife [21], divers [8], or providing reference signals for self-localization [4].

1.1 Related Work

This section briefly reviews current bedload tracers, trackers for wildlife monitoring, and related work in acoustic communication.

1.1.1 Bedload Tracers. Prior bedload tracers emitted electromagnetic beacon signals [14]. Liedermann [16] conducted an extensive study in Austria's Danube river using active radiotracers embedded in artificial stones as small as 27.5 mm (*b*-axis). The study achieved a high recovery rate of 96.3 % at mean water depths of 10 m, with detection ranges up to 200 m, and localization accuracy within 10 m to 15 m. However, RF tracers face challenges in locations where increased salinity—typically rising downstream[7]—causes higher attenuation of RF waves [3]. Therefore, alternative approaches are necessary for more saline rivers and oceanic environments.

WUWNET '24, October 28–31, 2024, Sibenik, Croatia

ACM ISBN 979-8-4007-1160-2/24/10
https://doi.org/10.1145/3699432.3699469

1.1.2 Wildlife Monitoring. Monitoring aquatic wildlife presents challenges similar to those in bedload tracing. Yang et al. [27] introduced an implantable beacon to track juvenile salmon, measuring 5.5x6.5x37 mm^3, which transmits acoustic signals at a carrier frequency of 416 kHz. However, this study primarily focused on monitoring the fish's vitals, with limited evaluation of detection and localization capabilities. Detection and communication were only validated in a 1.8 m tank, and the maximum distance of 400 m was only derived theoretically. The battery life was also limited to 30 days with a five-minute beacon interval.

Similarly, Saha et al. [21] documented a tracker for marine mammals with an acoustic communication range of up to 50 m. This device is relatively large (32x32x10 mm^3) and power-consuming, requiring up to 330 mW. Long-term monitoring necessitates regular recharging via an aluminum-air-salt-water energy harvesting system, which requires mammals to resurface regularly.

1.1.3 Underwater Communication. Many underwater communication modems deliver ranges up to tens of kilometers and precise localization with errors as low as 10 cm [6]. However, the devices are often prohibitively expensive, bulky, and power-hungry. The most suitable candidate for bedload tracers is the Nanomoden prototype V3 [22], which has a range up to 2 km and costs around 100 €. However, its size (60 mm x 42 mm diameter, excluding battery) and power consumption (1.5 W TX) exceed tracer requirements.

Backscattering acoustic underwater tags offer a promising alternative, potentially lasting indefinitely as they are powered wirelessly by a reader mounted on a ship [1, 15]. Wakeup ranges up to 100 m have been demonstrated [12], but they require arrays of large transducers (6.4 cm long, 6 cm diameter), which are too large for bedload tracers. In contrast, Bhardwaj [4] evaluated underwater backscatter communication using a small (3 cm diameter) piezo disk, but only achieved communication over several centimeters.

2 Implementation

Figure 1 illustrates the bedload tracer concept. The submerged tracer, powered by a battery and based on a microcontroller, transmits a beacon at regular intervals. This beacon signal is designed for detectability in noisy environments, unique identification among multiple tracers, and robust localization. The receiver, which is less constrained by size and cost, uses more electrical power and computational resources. It employs off-the-shelf commercial hydrophones to pick up the signals and a notebook computer for signal processing. Localizing the tracers requires a hydrophone array. While this work does not explore localization in detail, we propose a short-baseline system using time difference of arrival (TDoA). When hydrophones are placed close together, they can connect to the same sampling device, avoiding complex time-synchronization between multiple receivers. Additionally, TDoA with three or more hydrophones enables localization without relying on signal strength measurements, which can be unreliable if the line-of-sight component of the signal is blocked.

The remainder of this section describes first the beacon signal. We then compare the new tracer hardware with the prior, followed by a detailed description of the receiver and the software-defined signal processing chain.

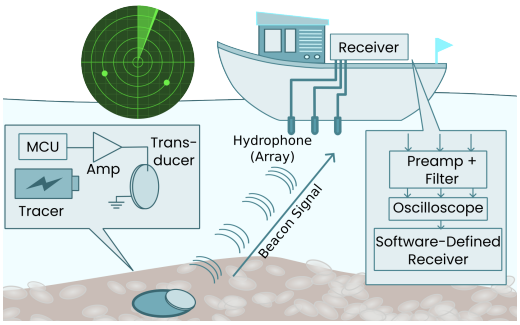

Figure 1: Concept sketch of the entire system. The tracer is submerged at the riverbed and transmits beacons regularly. The mobile receiver is mounted on a boat.

2.1 Acoustic Signal Design

The transmitted signal is designed to balance robustness against noise and distortions (e. g. , Doppler shift and multipath propagation), suitability for localization, distinguishability between tracers, and energy efficiency. We chose a carrier frequency of 70 kHz based on the transducer resonance. This frequency is a tradeoff between low attenuation at lower frequencies and transducer size, which increases with lower frequencies. Additionally, higher frequency ranges typically have less noise in rivers [13, 26].

Each beacon encodes a unique ID. We use a differential Phase-Shift-Keying (dPSK) modulated stream of N_s symbols with symbol interval T_s. We employ binary modulation, which is more energy-efficient than higher-order modulation schemes [18], to encode the unique ID, enabling distinguishing between 2^{N_s} tracers.

Doppler frequency shifts are significant at this carrier frequency: For example, a receiver traveling with 15 $km\,h^{-1}$ induces a frequency shift of approximately 650 Hz, which differential encoding alone can not compensate. To address this, we prepend the symbol stream with two preamble symbols. The observed frequency shift between the preamble symbols helps estimate the Doppler shift.

To enhance autocorrelation properties for localization and improve robustness against multipath propagation, we spread the symbol sequence with a 13-bit Barker code. While higher bandwidth improves autocorrelation, the transducer limits the maximum bandwidth. With the selected piezo disks, a bandwidth of 20 kHz is feasible. Thus, we set the codes's chip duration to 0.1 ms, resulting in a signal bandwidth of 60 kHz to 80 kHz. Since the tracer's ID remains constant throughout its lifetime, the signal samples are stored in the tracer's memory. Figure 2 illustrates the generation steps.

2.2 Tracer Hardware

A low-power and low-cost microcontroller (STM32L082KZ) generates the signal using its digital-to-analog converter (DAC). We use an off-the-shelf piezoelectric disk (PICeramics PRYY+0190 [19]), which has a diameter of 25 mm, a thickness of 2 mm, and nominal radial resonance frequency of 80 kHz. The disks are more affordable (≈ 6€) compared to professional hydrophones, often costing hundreds of euros. During prototyping, we mounted the piezo disk on a 3D-printed frame and coated it with a thin layer of epoxy

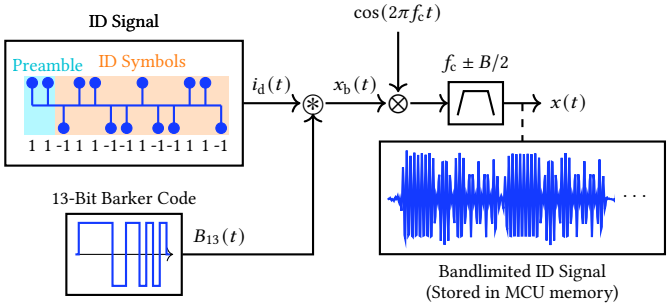

Figure 2: The beacon signal is a 2-dPSK modulated information signal, spread with a 13-bit Barker code, shifted to the carrier frequency, and bandlimited with a bandpass filter. For better visibility, signal durations are not scaled equally.

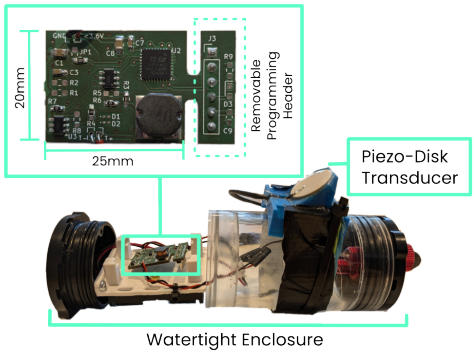

Figure 3: The prototype used for experiments in this work. The PCB and batteries are placed in a watertight tube. The self-made low-cost transducer is mounted outside the tube.

resin to protect the brittle material and isolate it electrically from the surrounding water. Figure 3 shows the prototype used in our experiments. The circuit board still has the potential for further miniaturization. The bulkiest part, however, is the inductor. In a productive tracer, the PCB, battery, and transducer would be cast with a resin to resemble the shape and weight of sediment particles. Without the enclosure, the tracer becomes very compact.

The large input impedance of piezoelectric transducers requires large driving voltages to generate sufficiently powerful acoustic signals that can be detected over long distances. However, the tracers are supplied by batteries with low voltages, i. e. , $V_{\text{bat}} = 3.6\,\text{V}$, which are available in various form factors to fit the size constraints. Therefore, an efficient driving circuit is required. This study compares and evaluates two approaches shown in Fig. 4. The circuit presented in our pilot study [18] uses a transformer to boost voltages four times, while the improved circuit uses a technique similar to a switching voltage regulator.

2.2.1 Transformer-based. In the transformer-based version, the DAC output is amplified, low-pass-filtered, and buffered using a single operational amplifier (Op-Amp), supplied directly from the battery (V_{bat}). We selected the AD8591 Op-Amp, which can drive

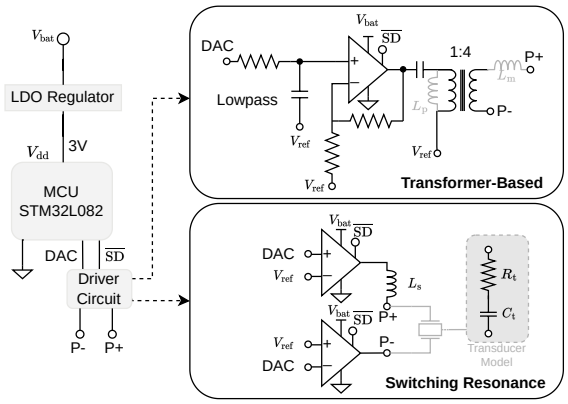

Figure 4: The two prototypes are both based on an STM32L082 microcontroller. The piezo driving circuits use different methods to generate the higher driving voltages for the transducers.

currents up to 250 mA and has a shutdown pin that limits current consumption to 100 nA when inactive, i. e. , between beacon intervals. The Op-Amp circuit includes a low-pass filter to smooth the DAC output and an amplifier to utilize the full battery voltage.

The selected ultrasonic sensing transformer (WA8351-AL [9]) quadruples the signal, achieving a maximum theoretical output amplitude of 14.4 V peak-to-peak (with $V_{\text{bat}} = 3.6\,\text{V}$). The transformer is compact, measuring 8.2 x 6.6 x 5.4 mm^3.

The transformer-based driving circuit can accurately reproduce the desired signal. The DAC allows the MCU to generate arbitrary signals, and the low-pass filter reduces higher-order frequency components, resulting in highly band-limited signals. However, a major disadvantage is the transformer's primary side parasitic inductance (L_p). Evaluation in [18] showed that most of the power consumed during transmission dissipates over the parasitic inductance, not contributing to signal power. Using transformers with higher inductance could reduce this loss but would significantly increase the size. Moreover, impedance matching with a second inductor L_m improves signal strength but adds a second bulky coil.

2.2.2 Switching-Resonance Based. This work's method is inspired by the piezo driver presented in [10]. It combines two techniques to increase the driving voltage on the piezo. First, it uses two switches to reverse the transducer's polarity, resulting in a peak-to-peak amplitude of $2V_{\text{bat}}$. These switches are implemented with Op-Amps (AD8591) in a comparator configuration, with one in inverting mode and the other in non-inverting mode.

To further increase the driving voltage, the circuit includes a series inductor (L_s) matched to the transducer. When driven near resonance, piezo transducers are typically modeled as a series capacitance (C_t) and resistance (R_t). The inductor functions similarly to a flyback inductor in a boost converter. When the amplifier output voltage is inverted, the current through the inductor continues to flow, building up higher voltages across the transducer terminals.

We matched the inductor by measuring the piezo's impedance in water at the carrier frequency, yielding $Z_p = (125.4 - j \cdot 171.3)\Omega$, and selected a 470 µH inductor. Although the match is imperfect, we observed substantial voltage gains, discussed in detail in Section 3.4.

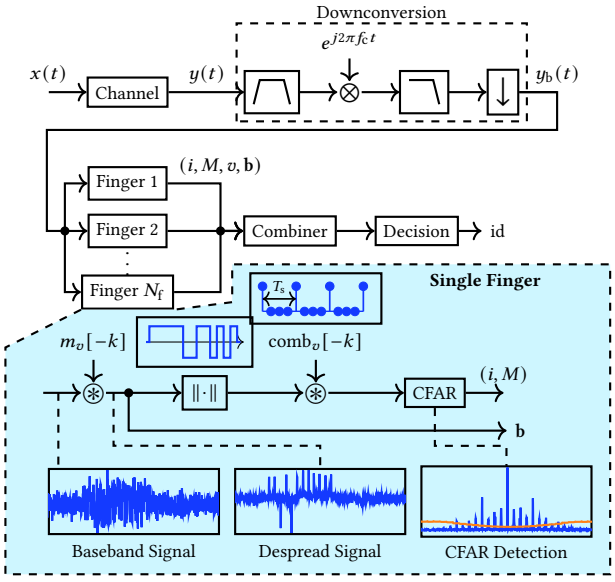

Figure 5: Signal processing in transmitter and receiver. The receiver uses multiple fingers, despreading and correlating with frequency-shifted versions of the spreading sequence to compensate for Doppler shifts.

This circuit is more efficient as it does not suffer from parasitic inductance. However, a drawback is that the amplifiers produce binary signals, which distribute some energy beyond the transmission bandwidth. The transducer's capacitance and the inductor act as a bandpass filter, somewhat attenuating frequencies outside the transmission band, but they cannot produce bandlimited signals as the transformer-based driver.

2.3 Receiver

The receiver is mobile and employs an omnidirectional hydrophone (AS-1, Aquamarin Scientific) to detect signals from the tracer. The analog module of the ahoi Modem [20] serves as a preamplifier, featuring a 16th-order bandpass filter with a passband between 50 kHz and 75 kHz and providing a total signal voltage gain of up to 96 dB. The output from the final amplifier stage is sampled using a USB oscilloscope (TiePie HS6 Differential) at a 2 MHz sampling rate and streamed to a laptop for subsequent signal processing in software.

2.3.1 Software-Defined Receiver. Figure 5 outlines the receiver's signal processing. The receiver first shifts the signal to baseband. It does this by filtering the signal through an 8-th order Butterworth bandpass filter with a passband between 60 kHz to 80 kHz, mixing it with a complex sinusoid at the carrier frequency, and filtering it again with a lowpass. After downconversion to baseband, the signal is downsampled to a baseband rate of $f_b = 40$ kHz, reducing processing power for the subsequent stages.

The following part of the receiver splits into multiple fingers, each correlating with a matched filter adapted to a specific Doppler shift, which leads to a rotation and sampling frequency mismatch of the baseband signal. Hence, the filters $m_v[k]$ are matched to a relative speed v between transmitter and receiver and correlate the baseband signal with

$$m_v[k] = B_{13}\left(k \cdot T_b\left(1 + \frac{v}{c}\right)\right) \cdot e^{j2\pi \cdot f_c \frac{v}{c} k T_b}, \tag{1}$$

with 13-bit Barker-sequence $B_{13}(t)$, sampling interval $T_b = 1/f_b$, and speed of sound c.

Correlation with the matched filters reduces noise. We further increase the SNR by leveraging the knowledge that N_s symbols are transmitted consecutively. Therefore, we take the correlation magnitude and correlate it with a comb signal

$$\text{comb}_v[k] = \sum_{i=0}^{N_s-1} \delta\left(k \cdot T_b \cdot \left(1 + \frac{v}{c}\right) - i \cdot T_s\right), \tag{2}$$

with dirac delta impulse $\delta(t)$. Due to the Doppler-induced sampling frequency offset, the comb signal is also adjusted to account for the velocity in each finger.

Due to the spreading code, the resulting signal contains distinct peaks when the beacon signal is present in the received samples. However, signal and noise powers can vary significantly. To detect peaks, we use a Constant False-Alarm Rate (CFAR) detector, originally introduced for radar pulse detection. The CFAR detector sets a dynamic threshold based on the noise power in the surrounding samples, multiplied by a constant factor, which adjusts the false alarm rate at the cost of sensitivity.

When a peak is detected, the finger returns the index i and the corresponding correlation value M. It also extracts the symbol samples in the despread signal $\mathbf{b} = [b_0, b_1, \ldots, b_{N_s}]$, whose phase differences contain the ID information.

Multiple fingers can detect the same beacon, and a single finger can detect multiple copies of a beacon due to multipath propagation. The combiner filters the detected beacons from all fingers, selecting only the beacon with the highest correlation M within a guard window. The size of this guard window is set equal to the message size in our prototype. To make the final ID decision, $\mathbf{b}$ is corrected for Doppler shifts, using the finger's velocity and the phase differences between the two preamble symbols as an estimate.

3 Evaluation

This section first evaluates robustness against Doppler frequency shifts and multipath propagation in a simulation study. We then estimate the effect of alignment between the piezo disk and the receiver's hydrophone by characterizing the disk's radiation pattern. Next, we measure the hardware prototype's current consumption and generated signal power for both piezo drivers, and estimate battery runtime. Finally, we describe a real-world experiment that measures maximum distances and error rates in a canal.

3.1 Simulation Setup

We performed the simulation in the equivalent baseband, and incorporated Doppler shifts, multipath propagation, and noise. We model a Doppler shift in baseband as a multiplication with the Doppler frequency f_d, and a sampling frequency offset by resampling the signal with rate r_d, i. e. ,

$$f_d = f_c \cdot \frac{v}{c} \quad \text{, and} \quad r_d = 1 + \frac{v}{c}. \tag{3}$$

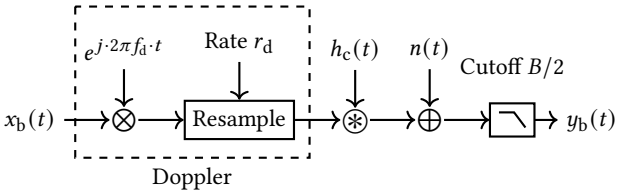

Figure 6: The simulation study in the equivalent baseband channel.

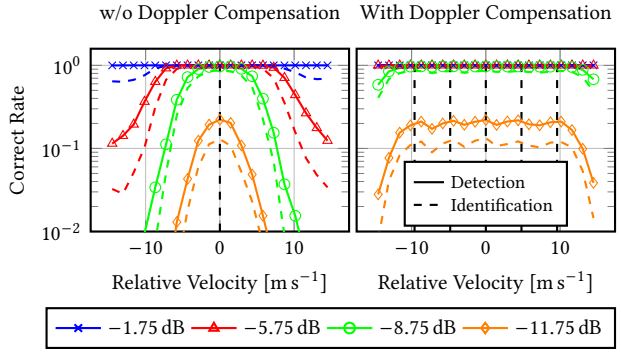

Figure 7: Detection and correct identification rates when a Doppler frequency shift is present in the signal at different SNRs, once with a single matched filter for Doppler-free signals (left) and with five matched filters (right).

We then convolve the Doppler-shifted signal with a channel impulse response $h_c(t)$ and add white Gaussian noise $n(t)$. Finally, the signal is filtered with an 8-th-order lowpass filter with cutoff frequency $B/2$, resembling the filters in the receiver. In the following simulations, we used a sampling rate of 40 kHz and a lowpass filter cutoff frequency of $B/2 = 10$ kHz, and assumed $c = 1450\,\mathrm{m\,s^{-1}}$.

When evaluating robustness, three error types may arise: *False alarms* occur when a beacon is detected although none was transmitted (false-positive), *misses* occur when a beacon is transmitted but not detected (false-negative), and *misidentifications* occur when a transmitted beacon is detected, but the ID is decoded incorrectly. The false-alarm rate depends solely on the detection threshold in the CFAR detector and is independent of Doppler shifts or channel impulse responses. The miss-rate and misidentification rate, which we investigate in the next section, are influenced by Doppler shifts and multipath propagation.

3.2 Robustness against Doppler Shifts

Figure 7 shows the rate of successfully detected beacons using two different methods: one with a single matched filter for Doppler-free signals, and another with five matched filters for velocities of $\pm 9.6\,\mathrm{m\,s^{-1}}$, $\pm 4.8\,\mathrm{m\,s^{-1}}$, and $0\,\mathrm{m\,s^{-1}}$. In both cases, we simulated 2000 beacons per data point with 10 ID symbols. The tested velocities range from $-14.5\,\mathrm{m\,s^{-1}}$ to $14.5\,\mathrm{m\,s^{-1}}$.

Without compensation, many beacons are missed as soon as a Doppler shift is present, especially at low SNRs. This is expected because the maximum correlation between the received and expected signal decreases when the received signal is distorted, making it less likely to exceed the CFAR detector's threshold. However, with five matched filters, packet miss rates are nearly independent of Doppler shift over the investigated range, with increases in miss rates only at lower SNRs and the highest velocities. Regardless of Doppler compensation, beacons start to be missed when the SNR drops below −8 dB, with only 20 % of beacons detected at −11.75 dB. We chose a CFAR threshold of four, i. e. , the correlation must exceed four times the noise power, leading to less than one false alarm per hour. Reducing the threshold slightly improves detection rates, but also leads to more false alarms, which is decouraged.

Correct identification rates are similarly influenced by Doppler shifts. The rate of correctly identified beacons is slightly lower than the detection rate. However, at SNRs higher than −5.75 dB, nearly all beacons are correctly identified.

3.2.1 Multipath Propagation. In underwater communication, multipath propagation often severely limits the reliability of communication links. We evaluate the robustness of our tracer in five real-world channels recorded in a small marina in Hamburg. The recording procedure, environment, and channel characteristics are detailed in [24], in which the channels are named *CASTLE 1-5*. These channels feature numerous short-distance obstacles, resulting in moderate multipath propagation. Our prior experience on the Rhine River and findings from the Hudson River [5] suggest that channels on large rivers are much more benevolent.

Interestingly, the correct identification rate in the simulated multipath channels was not significantly worse than in an ideal frequency-flat channel. The wideband transmitted signals demonstrate robustness against multipath effects. However, the real-world tests in Section 3.5 show that both detection and identification rates suffer in more challenging multipath environments.

3.3 Transducer Characteristics

The cost-effective disk-shaped piezo transducers do not emit an omnidirectional signal, which may pose a challenge if signal strength varies significantly with misalignment between the receiver and transmitter. To address this, we measured the transducer's directivity to estimate the dependence of signal strength on disk orientation.

We carried the measurement out in a nearby canal in Hamburg on a quiet, windless day. The channel is approximately four meters deep. We attached an omnidirectional hydrophone (Aquarian AS-1 [2]) and the piezo disk to a floating frame, shown in Fig. 8 (left), so that both were 36 cm apart from each other, and about one meter below the water surface. As in the prototype, the disk was attached to a 3D-printed frame and coated with a thin layer of epoxy resin.

To change the disk's orientation during the experiment, it was mounted on a shaft connected to a stepper motor. We emitted signals with the disk and received them with the AS-1 hydrophone. Signal generation and recording were synchronized using a TiePie HS-5 combined signal generator and oscilloscope. The hydrophone's signal was preamplified with an Aquarian PA-6 preamp with a 20 dB gain.

To estimate the transmitted signal's strength, we aimed to capture the direct Line of Sight (LoS) path. However, reflections from quay walls and the water surface could significantly distort the measurements. To isolate the LoS path, we emitted a 200 ms linear

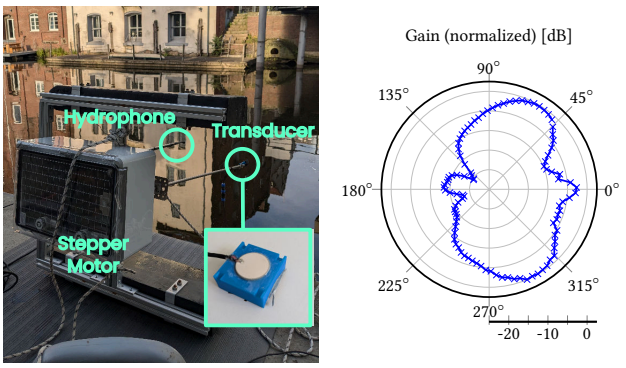

Figure 8: A floating device (left) mounts the transmitting piezo disk and a receiving hydrophone while changing the disk's orientation. The signal strength (normalized) depends on the disk's orientation (right).

chirp in the range of 50 kHz to 90 kHz. The chirp has favorable autocorrelation properties, enabling good separability of the LoS signal from delayed reflections [25]. The maximum correlation magnitude within a propagation delay between 180 µs to 317 µs was taken as signal strength. This delay corresponds to travel distances from transmitter to receiver of 26 cm to 46 cm—much shorter than the shortest reflection paths.

Figure 8 (right) shows the normalized signal strength from 0 to 360°. We transmitted five chirps for each angle and averaged the correlation peaks. The orientation normal to the receiver corresponds to zero degrees. Interestingly, the strongest signal is not observed around zero degrees; instead, they appear around ±50°. This could be because we are exciting the transducer close to its radial resonance frequency rather than its thickness-direction resonance, which is approximately 1 MHz.

In the front half of the transducer, we observe a variation of up to 10 dB in signal strength between the strongest and weakest directions. The back of the transducer transmits a signal up to −20 dB weaker than the strongest paths on the front, likely due to the transducer's mounting: The 3D-printed frame is hollow and contains air, reflecting most of the signal. A fully casted tracer would not contain such an air inclusion and likely performs better also on its backside.

3.4 Signal Power and Power Consumption

Transmitting a high-power signal is crucial for robust detection over long distances. To evaluate the effectiveness of the resonance-switching driver compared to the previously used transformer-based driver, we measured the power dissipated over the transducer during transmission. We recorded the voltage $v_t(t)$ and current $i_t(t)$ through the transducer and derived the dissipated power averaged over an entire beacon duration T_s as follows:

$$P_s = \frac{1}{T_s} \int_0^{T_s} v_t(t) \cdot i_t(t)\, \mathrm{d}t\,. \tag{4}$$

We used an oscilloscope to observe v_t, and i_t over a 10 Ω shunt resistor. The driver circuit was supplied $v_{bat} = 3.9$ V. Along with the resonance-switching driver, we tested the transformer-based driver with and without impedance matching with the same 470 µH inductor described in Section 2.2.2. Table 1 shows the measured signal power and peak-to-peak signal voltages over the same transducer.

Table 1: Signal power and peak-to-peak signal voltages with the transformer-based piezo driver with and without a matching inductor and the new resonance-switching driver.

Piezo Driver	Sig. Power	Amplitude
Transformer (unmatched)	6.81 mW	6.0 V
Transformer (matched)	14.35 mW	9.25 V
Switching-Resonance	53.5 mW	15.8 V

The switching-resonance driver achieved the highest signal power at 53.5 mW, nearly eight times larger than the unmatched prototype and 3.7 times larger than the transformer-based driver with impedance matching. This corresponds to a 9 dB gain in signal power, which helps achieve longer communication distances, as validated in the real-world experiment described in Section 3.5.

3.4.1 Power Consumption. Long battery runtime is essential for the tracers, making the piezo driver's efficiency crucial to balance signal power with low power consumption. To measure efficiency and estimate total battery runtimes, we evaluate the prototype's power consumption using the battery voltage $v_{bat}(t)$ and current $i_{bat}(t)$, yielding the instantaneous power consumption:

$$p_{bat}(t) = v_{bat}(t) \cdot i_{bat}(t)\,. \tag{5}$$

By recording power consumption over a complete duty cycle, we can determine consumption in every prototype state, such as deep sleep, running, and transmitting. To accurately detect microampere currents during deep sleep, we used a 100 Ω shunt resistor and an active probe with 10x gain. For larger currents during active transmission, we used a smaller 10 Ω shunt resistor.

Figure 9 shows the recorded power consumption of the prototype with both piezo driver circuits. The driver circuit affects power consumption only during active transmission. The power consumption during deep sleep is about 20 µW. When the MCU is active but not yet transmitting, it is about 7.5 mW. During active transmission, the switching-resonance driver consumes roughly 60 mW, exceeding the MCU active power by about 53 mW—matching the signal power dissipated over the transducer. This match indicates that the switching driver is highly efficient.

In contrast, the transformer-based piezo driver is less efficient. The power consumption exceeds the pure MCU's consumption by approximately 64 mW, while the signal power is 14.35 mW. Thus, only 22 % of the expended power is utilized for signal generation; the rest is dissipated within the driver circuit, likely due to the transformer's parallel inductance.

3.4.2 Battery Runtime. Using the power consumption measurements, we estimate the tracer's runtimes. Figure 10 shows the battery lifetime of the more efficient switching-resonance driver when generating a 10 ID-symbol signal, distinguishing between up to 1024 unique tracers. Depending on the tracer size constraints, different battery types are viable. The smallest tracers may utilize two CR1632 coin cells, reaching 284 days runtime with a beacon transmitted every 10 seconds. Larger tracers may utilize a 3.7 V

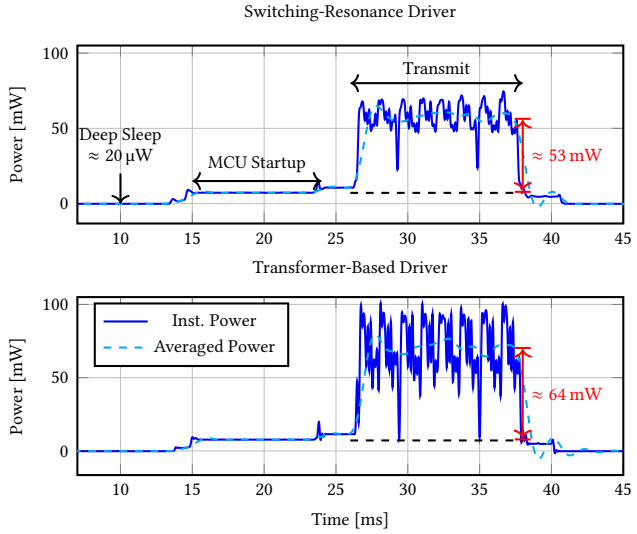

Figure 9: The prototype's power consumption over a duty cycle transmitting an 8-symbol sequence with a switching-resonance driver and the transformer-based driver with frequency matching.

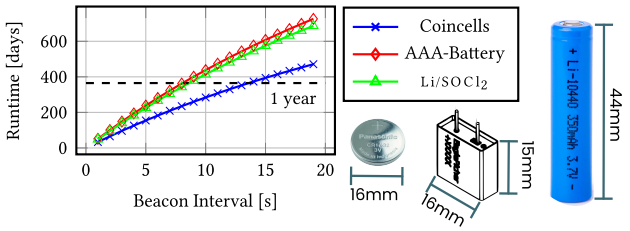

Figure 10: Estimated runtimes based on the power consumption measurements with two coin cells (type CR1639), a 3.7V AAA battery (ANSI 10440), and with a high energy-density special purpose Lithium Thyonide Chloride battery [11].

AAA-shape battery, at which it can reach up to 438 days at the same beacon interval. Moreover, special purpose batteries, e. g. , a $Li/SOCl_2$ battery, can deliver a similar runtime at only 40 % of the volume compared to the AAA battery.

3.5 Real-World Distances

To validate the tracer in a real-world scenario, we deployed a prototype in a canal in Hamburg, the transducer oriented towards the canal opening. It was placed roughly 1.5 m below the water surface in 4 meter deep water. We positioned the receiver at seven different locations along the canal at distances up to 390 m, as shown in Fig. 11 (left). The canal contained many reflectors, e. g. , small boats, jetties, a bridge pillar, and smooth stone walls.

The prototype transmitted a beacon every second, and we recorded the received signals for about 120 s at each location. The SNRs of detected beacons, shown in Fig. 11 (right), exhibit a clear trend, ranging from up to 18 dB at 90 m to −9 dB at 390 m. However, multipath propagation posed challenges in the canal environment. Some beacons were detected multiple times at distances below 200 m,

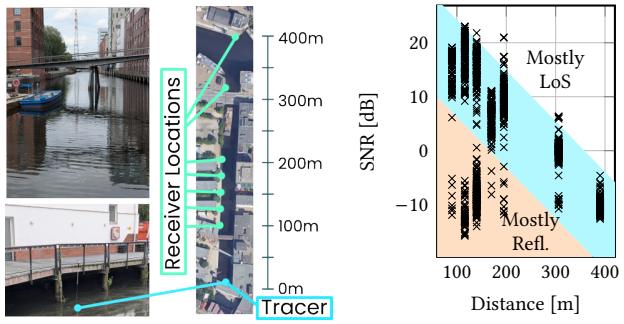

Figure 11: The realworld validation took place in a 20 m-wide canal (left) with distances up to 400 m. With rising distance, the SNR of received packets drops (right). Reflections are received with lower SNRs.

arriving via different reflection paths, which resulted in detections with significantly lower SNR and frequent ID mis-detections. At longer distances, reflections were likely present but too weak to be detected by the receiver.

Figure 12 (left) shows the rate of detected and correctly identified beacons relative to the total number of transmitted beacons. In ranges below 300 m, more beacons are detected than transmitted due to multiple detections in the multipath channel, with correct identification rates around 90 %. At the maximum distance, only 61 % of the transmitted beacons are detected, and the correct identification rate drops to 12 %.

Comparing these detection rates with the simulation results from Section 3.2, the poor detection rate aligns with the simulated rates at such low SNRs. However, with higher SNR, the error rates exceed those in the simulation, likely due to the heavy multipath characteristics of the canal. Multipath propagation leads to two types of errors: Propagation paths with a delay longer than the beacon duration lead to multiple detections of the same beacon. In contrast, paths with close delay compromise the correct identification, even when the SNR is high. Large rivers typically have more favorable channels due to their larger width and diffuse riverbed. Figure 12 (right) illustrates the signal after despreading once at the Rhine river (from our prior study) and once in the canal. In the river, distinct correlation peaks are clearly visible, while the canal signal is more complex, showing many peaks of similar height.

4 Discussion and Conclusion

Bedload tracers are crucial for monitoring waterways, but current RF-based tracers are ineffective in deep waters or high-salinity rivers. Our previous pilot study demonstrated the feasibility of affordable, small, and low-power acoustic tracers but highlighted their inadequate signal strength in noisy conditions. This work introduces an alternative piezo driver that is simpler and generates nearly four times the signal power while consuming less energy.

Our simulations and real-world tests show that the receiver with matched filters is robust against Doppler frequency shifts and moderate multipath propagation. We confirmed that the cost-effective disk-shaped transducers have at most a −10 dB directivity loss when misaligned with the receiver. In real-world canal tests, we successfully detected transmitted beacons from up to 400 m, effectively

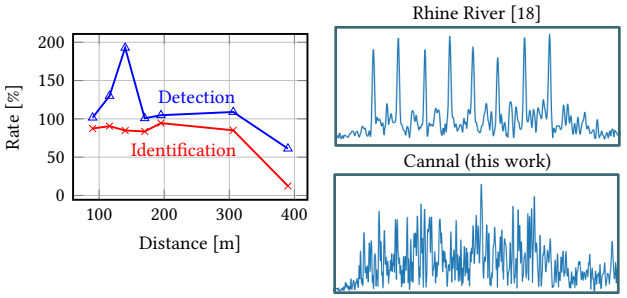

Figure 12: Correct detection and identification rates relative to the number of transmitted beacons (left). The multipath propagation leads to heavily distorted signals (right). Large rivers experience much less reflections.

doubling the range of the previous prototype. However, we also observed that heavy multipath environments remain challenging.

The presented prototype meets the requirements for bedload tracers effectively: it is compact, with dimensions of 20x25x8 mm^3, and has potential for further miniaturization. It can operate for up to a year with a 15-second interval between beacons using a coin cell battery, and it is cost-effective, with components, including the transducer, costing about 15 €.

The receiver still offers room for improvement. For instance, implementing a hydrophone array can increase the SNR of the received signal and enhance robustness against river noise and multipath. Additionally, the software-defined receiver could incorporate an equalizer or rake receiver to further mitigate multipath effects. We also see significant potential for a minimalistic beacon transmitter in other applications, such as tracking divers, underwater sensors, or other equipment, or long-lasting and affordable anchors for localization.

In conclusion, this work advances the development of acoustic bedload tracers, providing a more powerful and efficient solution for monitoring complex aquatic environments.

References

[1] Sayed Saad Afzal, Waleed Akbar, Osvy Rodriguez, Mario Doumet, Unsoo Ha, Reza Ghaffarivardavagh, and Fadel Adib. 2022. Battery-free wireless imaging of underwater environments. *Nature Communications* 13, 1 (2022). https://doi.org/10.1038/s41467-022-33223-x

[2] Aquarian. 2024. AS-1 Hydrophone. https://www.aquarianaudio.com/as-1-hydrophone.html. Retreived 2024-05-03.

[3] Vasily Artemov. 2021. The Interaction of Electromagnetic Waves with Water. In *The Electrodynamics of Water and Ice*. Springer. https://doi.org/10.1007/978-3-030-72424-5_2

[4] Ananya Bhardwaj, Ahmed Allam, Alper Erturk, and Karim G. Sabra. 2023. Ultrasound-Powered Wireless Underwater Acoustic Identification Tags for Backscatter Communication. *IEEE Trans. on Ultrasonics, Ferroelectrics, and Frequency Control* (2023). https://doi.org/10.1109/TUFFC.2023.3344638

[5] Brian Borowski. 2009. Characterization of a very shallow water acoustic communication channel. In *OCEANS 2009* (2009-10). https://doi.org/10.23919/OCEANS.2009.5422360

[6] Filippo Campagnaro, Fabian Steinmetz, Bernd-Christian Renner, and Michele Zorzi. 2024. Affordable underwater acoustic modems and their application in everyday life: a complete overview. In *Proc. of the 17th International Conference on Underwater Networks & Systems*. https://doi.org/10.1145/3631726.3631734

[7] Miguel Cañedo-Argüelles, Ben J. Kefford, Christophe Piscart, Narcís Prat, Ralf B. Schäfer, and Claus-Jürgen Schulz. 2013. Salinisation of rivers: An urgent ecological issue. *Environmental Pollution* 173 (2013). https://doi.org/10.1016/j.envpol.2012.10.011

[8] Tuochao Chen, Justin Chan, and Shyamnath Gollakota. 2022. Underwater messaging using mobile devices. In *Proc. of the ACM SIGCOMM 2022 Conference*. https://doi.org/10.1145/3544216.3544258

[9] Coilcraft. 2021. WA8351-AL Ultrasonic Transformer. https://www.coilcraft.com/getmedia/3a8a29e3-84c9-497d-9acd-96ca699b92c2/wa8351-AL.pdf. Retreived 2024-07-07.

[10] Z. D. Deng, T. J. Carlson, H. Li, J. Xiao, M. J. Myjak, J. Lu, J. J. Martinez, C. M. Woodley, M. A. Weiland, and M. B. Eppard. 2015. An injectable acoustic transmitter for juvenile salmon. *Scientific Reports* 5, 1 (2015). https://doi.org/10.1038/srep08111

[11] Eaglepitcher. 2024. 350 mAh Li/SOCl2 Battery Datasheet. https://www.eaglepicher.com/sites/default/files/LTC-3PN-M10523.pdf. Retreived 2024-07-16.

[12] Aline Eid, Jack Rademacher, Waleed Akbar, Purui Wang, Ahmed Allam, and Fadel Adib. 2023. Enabling Long-Range Underwater Backscatter via Van Atta Acoustic Networks. In *Proc. of the ACM SIGCOMM 2023 Conference*. ACM. https://doi.org/10.1145/3603269.3604814

[13] Thomas Geay, Ludovic Michel, Sébastien Zanker, and James Robert Rigby. 2019. Acoustic wave propagation in rivers: an experimental study. *Earth Surface Dynamics* 7, 2 (2019). https://doi.org/10.5194/esurf-7-537-2019

[14] H. M. Habersack. 2001. Radio-tracking gravel particles in a large braided river in New Zealand: a field test of the stochastic theory of bed load transport proposed by Einstein. *Hydrological Processes* 15, 3 (2001). https://doi.org/10.1002/hyp.147

[15] Junsu Jang and Fadel Adib. 2022. Underwater Backscatter Networking. In *Proc. of the ACM SIGCOMM 2022 Conference*. https://doi.org/10.1145/3341302.3342091

[16] Marcel Liedermann, Michael Tritthart, and Helmut Habersack. 2013. Particle path characteristics at the large gravel-bed river Danube: results from a tracer study and numerical modelling. *Earth Surface Processes and Landforms* 38, 5 (2013).

[17] Nda Muhammad, Mohd Shalahuddin Adnan, Mohd Azlan Mohd Yosuff, and Kabiru Abdullahi Ahmad. 2019. A review of field methods for suspended and bedload sediment measurement. *World Journal of Engineering* 16, 1 (2019). https://doi.org/10.1108/WJE-07-2018-0226

[18] Peter Oppermann and Bernd-Christian Renner. 2024. Towards Cost-Effective Acoustic Tracers for Bedload Transport Measurement. In *Underwater Communications and Networking (UCOMMS'24)*. Accepted for Publication.

[19] PICeramic. 2024. Piezoelektrische Scheiben. https://www.piceramic.de/fileadmin/user_upload/physik_instrumente/files/datasheets/PRYY-Datenblatt.pdf. Retreived 2024-05-03.

[20] Bernd-Christian Renner, Jan Heitmann, and Fabian Steinmetz. 2020. AHOI: Inexpensive, low-power communication and localization for underwater sensor networks and μAUVs. *ACM Trans. on Sensor Networks (TOSN)* 16, 2 (2020).

[21] Swapnil Sayan Saha, Caden Davis, Sandeep Singh Sandha, Junha Park, Joshua Geronimo, Luis Antonio Garcia, and Mani Srivastava. 2024. LocoMote: AI-driven Sensor Tags for Fine-Grained Undersea Localization and Sensing. *IEEE Sensors Journal* (2024). https://doi.org/10.1109/JSEN.2024.3383721

[22] Benjamin Sherlock, Nils Morozs, Jeffrey Neasham, and Paul Mitchell. 2022. Ultra-Low-Cost and Ultra-Low-Power, Miniature Acoustic Modems Using Multipath Tolerant Spread-Spectrum Techniques. *Electronics* 11, 9 (2022). https://doi.org/10.3390/electronics11091446

[23] Arvind Singh, Zi Wu, Peter Wilcock, and Efi Foufoula-Georgiou. 2023. Experimental Observations of Bedload Tracer Movement: Effects of Mixed Particle Sizes and Bedforms. *Water Resources Research* 59, 5 (2023). https://doi.org/10.1029/2022WR033114

[24] Fabian Steinmetz and Bernd-Christian Renner. 2021. From the Long-Range Channel in the Ocean to the Short-Range and Very Shallow-Water Acoustic Channel in Ports and Harbors. In *2021 Fifth Underwater Communications and Networking Conference (UComms)*. https://doi.org/10.1109/UComms50339.2021.9598094

[25] Fabian Steinmetz and Bernd-Christian Renner. 2022. Taking LoRa for a Dive: CSS for Low-Power Acoustic Underwater Communication. In *2022 Sixth Underwater Communications and Networking Conference (UComms)*. https://doi.org/10.1109/UComms56954.2022.9905674

[26] Miodrag S. Vračar and Miomir Mijić. 2011. Ambient noise in large rivers. *The Journal of the Acoustical Society of America* 130, 4 (2011). https://doi.org/10.1121/1.3628666

[27] Yang Yang, Jun Lu, Brett D. Pflugrath, Huidong Li, Jayson J. Martinez, Siddhartha Regmi, Bingbin Wu, Jie Xiao, and Zhiqun Daniel Deng. 2022. Lab-on-a-Fish: Wireless, Miniaturized, Fully Integrated, Implantable Biotelemetric Tag for Real-Time In Vivo Monitoring of Aquatic Animals. *IEEE Internet of Things Journal* 9, 13 (2022). https://doi.org/10.1109/JIOT.2021.3126614